



Cite this: DOI: 10.1039/d5mh00937e

Received 17th May 2025,
Accepted 23rd June 2025

DOI: 10.1039/d5mh00937e

rsc.li/materials-horizons

Emergent multiferroicity in two-dimensional electron gas of complex oxides for FET-based artificial synaptic junctions†

Mohammad Karbalaei Akbari,^a Yanbin Cui,^b Christophe Detavernier^a and Serge Zhuiykov^{*ab}

Designing multifunctional nanoarchitectures that integrate distinct physical phenomena is paramount for next-generation electronics. Here, we report the emergence of a two-dimensional electron gas (2DEG) coexisting with robust multiferroicity at complex oxide hetero-interfaces. Synthesized via atomic layer deposition (ALD), these ultrathin heterostructures comprise a ferroelectric $\text{Ti}_{0.6}\text{Sn}_{0.4}\text{O}_2$ layer coupled with ferromagnetic Cr-doped SnO_2 . This unique integration engenders strong spin–charge–lattice interactions within the 2DEG, driven by the coupling between switchable ferroelectric domains and itinerant ferromagnetism. Piezoresponse force microscopy confirms tunable ferroelectric polarization, while magnetotransport measurements, including clear Shubnikov–de Haas oscillations, reveal high-mobility quantum transport within the 2DEG. Critically, the heterostructure exhibits dynamic capacitive-to-inductive transitions and current-induced polarization switching, characteristic of ferroelectric memristive behavior suitable for FET-based artificial synaptic junctions. Programmable pulse transient current responses demonstrate the potential for emulating synaptic plasticity. These findings unveil an all-oxide platform uniquely combining ferroelectricity, ferromagnetism, memristive switching, and quantum transport, paving the way for novel spin-orbitronic devices and energy-efficient neuromorphic computing architectures.

New concepts

This work introduces the breakthrough development of multiferroic field-effect transistor (FET)-based artificial synaptic junctions, uniquely enabled by an emergent two-dimensional electron gas (2DEG) exhibiting intrinsic multiferroicity. Achieved through precise nanofabrication and advanced materials characterization, this innovation hinges on interface-tailored elemental profile engineering within atomically thin Cr-doped $\text{SnO}_2/\text{Ti}_{0.6}\text{Sn}_{0.4}\text{O}_2/\text{TiO}_2$ complex oxide heterointerfaces. These engineered interfaces stabilize the coexistence of ferroelectric and ferromagnetic orders within the conductive 2DEG channel, mediated by interfacial oxygen vacancies and mixed-valence Ti^{3+} states. Our approach directly leverages the strong electric-field-mediated coupling of these ferroic orders for synaptic functionality, including short- and long-term plasticity and reliable performance—key metrics for neuromorphic computing. Unlike prior research relying on separate material layers or singular ferroic phenomena, our all-oxide platform unifies multiferroicity, memristive behavior (evidenced by dynamic capacitive-to-inductive transitions), and quantum transport into a single architecture. This differentiation is enabled by meticulous control over interfacial chemistry and structure at the nanoscale, offering transformative insights into the design of emergent functionalities. By bridging oxide electronics, spin-orbitronics, and adaptive computing, this work establishes a scalable paradigm for energy-efficient neuromorphic systems and spintronic devices with electrically tunable, coupled physical states.

Introduction

The electronic modulation of magnetic states is one of the primary principles of multiferroics, providing unprecedented opportunities for the emergence of spintronic nanoelectronics,

and stimulating fascinating opportunities for data and information processing beyond the binary concepts. Among the various nanostructures, multiferroic oxide heterointerfaces, exhibiting emergent formation of 2DEGs with coupled spintronic properties, represent a frontier in materials science and condensed matter physics.^{1,2} The emergence of topological polar complexes at oxide heterointerfaces represents captivating advancement of multiferroic systems.^{3,4} Particularly, the confluence of ferroelectricity and ferromagnetism at such interfaces enables the creation of topologically non-trivial polar textures, offering unprecedented control over electronic and magnetic states.^{5–7} The resulting polar topological nanotextures have gained significant attention among researchers due to their switchable polar nanoscale characteristics, making

^a Department of Solid-State Sciences, Faculty of Science, Ghent University, Krijgslaan 281/S1, Ghent, Belgium. E-mail: Mohammad.akbari@ugent.be, Serge.zhuiykov@ugent.be

^b Center for Green Chemistry & Environmental Biotechnology, Ghent University Global Campus, Incheon 21985, South Korea

^c Institute of Process Engineering, Chinese Academy of Sciences, Beijing 100190, China

† Electronic supplementary information (ESI) available. See DOI: <https://doi.org/10.1039/d5mh00937e>



them attractive candidates for the development of ultrahigh-density nanoelectronic circuits.^{8,9} The electrical stimulation of these complex polar textures activates polar domains with intricate topologies, arising from the interplay between electrostatic forces, polar gradients, and material design.¹⁰ Specifically, incorporating ferroelectric semiconductors with spontaneous out-of-plane polarization can tune in-plane electronic transport *via* gate voltage or modulate resistive switching in a polarization-dependent way.^{11,12} In the context of nanofabrication, multiferroic epitaxial structures are considered optimal for integration into nanoelectronic systems.¹⁰ Bottom-up fabrication techniques offer potential solutions to the challenges of epitaxial growth of multiferroic structures with switchable topological features.¹¹ Nonetheless, the engineering of specific spintronic structures remains a fundamental challenge, hindering the widespread application of epitaxial ferroelectric nanoelectronic films.¹²

The realization of switchable polar characteristics in few-nanometer thin epitaxial multiferroic complex metal oxides remains a largely unexplored area.¹³ In this work, we specifically report the fabrication of field effect transistor (FET) artificial synaptic junctions based on a multiferroic 2DEG system. This system is based on the epitaxial integration of $\text{Ti}_{0.6}\text{Sn}_{0.4}\text{O}_2$ and Cr-doped SnO_2 films offering the benefit of

inherent multiferroic control of the 2DEG within a robust metal oxide heterostructure (Fig. 1a). These structures were fabricated *via* sequential atomic layer deposition (ALD), a technique well suited for the precise synthesis of complex metal oxides¹⁴ including tin titanate films.¹⁵ The deposition sequence consisted of Cr-doped SnO_2 (ferromagnetic layer), $\text{Ti}_{0.6}\text{Sn}_{0.4}\text{O}_2$ (ferroelectric interlayer, Fig. 1b), and TiO_2 (oxide gate). Subsequent post-treatment of the fabricated heterointerfaces enabled precise control over vacancy content, doping concentration, and electronic properties, resulting in piezoelectricity and tunable artificial synaptic functionalities. A critical aspect requiring further investigation is the controlled formation and functional contribution of the $\text{Ti}_x\text{Sn}_{1-x}\text{O}_2$ interlayer in optimizing overall multiferroic film performance.

Here, the electromagnetic control of 2DEGs was achieved owing to the presence of ferromagnetically polarized $\text{Ti}_{0.6}\text{Sn}_{0.4}\text{O}_2/\text{Cr-doped SnO}_2$ heterointerfaces. Particularly, interfacial elemental diffusion at the heterointerfaces resulted in the development of ferroelectric domains with polarization-dependent characteristics,¹⁶ leveraging electric-field induced polarization and corresponding non-linear resistance changes in two-terminal memristor and FET synaptic devices. Characterization techniques revealed the key role of elemental Sn^+ accumulation

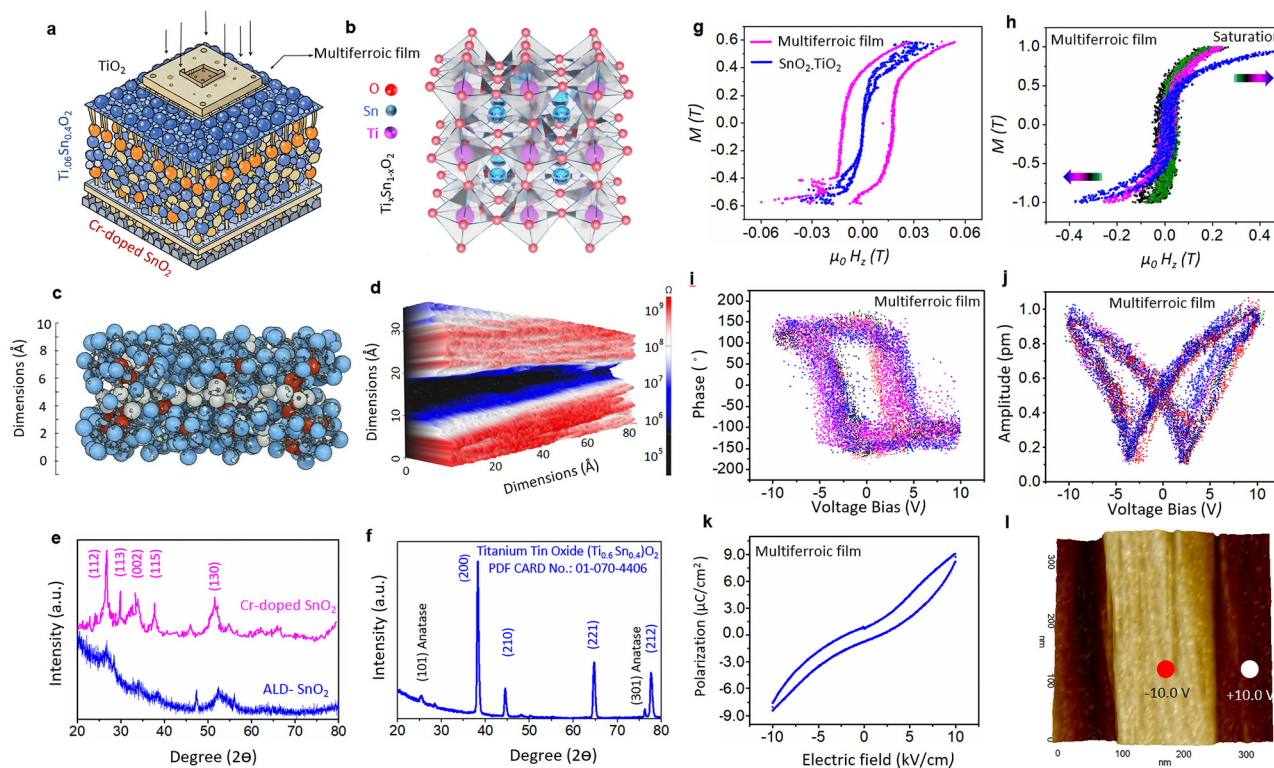


Fig. 1 (a) Schematic illustration images of the Cr-doped $\text{SnO}_2/\text{Ti}_{0.6}\text{Sn}_{0.4}\text{O}_2/\text{TiO}_2$ heterostructures. (b) The 3D crystalline structure of $\text{Ti}_{0.6}\text{Sn}_{0.4}\text{O}_2$. (c) The formation of 2DEGs at the heterointerface and (d) its corresponding c-AFM resistance profile image of the heterojunction. (e) The XRD characteristics of SnO_2 and Cr-doped SnO_2 films. (f) The XRD structural features of the resulting $\text{Ti}_{0.6}\text{Sn}_{0.4}\text{O}_2$ crystalline heterostructure after thermal annealing. (g) The magnetization features of the Cr-doped SnO_2 film. (h) The effect of the magnetization of multiferroic film. (i) Selected piezoresponse hysteresis loops (selected from 100 cycles). (j) The cyclic piezoresponse amplitude butterfly loops (selected from 100 cycles) exhibit the voltage-dependent response, reflecting the tunable characteristics. (k) The polarization vs. the electric field at room temperature. (l) The typical PFM image map of polarized domains.



at the complex metal oxide heterointerface, which creates a charged interface (Fig. 1c). The trace of a highly conductive 2DEG layer was observed by *c*-AFM (Fig. 1d). Through materials design, advanced characterization, and multiscale simulations, this study elucidates the pivotal role of interfacial elemental distribution in orchestrating ferroelectric domains with polarization-dependent transport, non-linear resistive switching, and ultimately, the emergence of a multiferroic 2DEG with temperature-dependent mobility characteristics. The surprising revelation of a capacitance-to-inductance (C–L) transition in memristive devices further unlocks synaptic functionalities that transcend the conventional resistive switching paradigm. Our findings bridge the gap between robust 2DEG quantum transport and deterministic polarized control within atomically precise platforms, advancing the integration of epitaxial ferroelectric nanostructures into next-generation spintronic and neuromorphic architectures.

Results and discussion

Ferromagnetic characteristics

The fabrication process began with the deposition of a 10 nm Cr-doped SnO₂ film in an O₂ plasma on electrodes using PEALD. Chromium incorporation was achieved through a supercycle ALD approach, and the resulting film was subsequently annealed at 400 °C in a forming gas (99.9% N₂). Cr interdiffusion throughout the SnO₂ film was observed following the annealing step, a finding confirmed by X-ray photoelectron spectroscopy (XPS) profiling (Fig. S1, ESI†). Subsequent PEALD of Ti_xSn_{1-x}O₂ and TiO₂ layers was performed on the Cr-doped SnO₂ sublayer. The Cr-doped SnO₂/Ti_{0.6}Sn_{0.4}O₂ film, which serves as a multiferroic heterostructure, will be consistently referred to as such in the following discussion.

Micro-Raman spectroscopy revealed the vibration characteristics peaks at 124, 396, 623, and 792 cm⁻¹ were assigned to the B_{1g}, A_{2g}, A_{1g}, and B_{2g} vibrational modes of Sn–O, respectively,^{17,18} while the B_{1g} peak of TiO₆-octahedra was observed at 196 cm⁻¹ (Fig. S2, ESI†).¹⁹ Importantly, XPS analysis indicated that most of the Cr ions existed in the Cr³⁺ oxidation state,²⁰ confirming that the three unpaired 3d electrons of Cr³⁺ ions introduce localized magnetic moments (~3μ_B per Cr³⁺).²¹ The diluted Cr doping with concentrations in the 5–10% range, promotes spatial separation of Cr ions in the SnO₂ lattice, potentially favoring ferromagnetism.^{21,22} Cr³⁺ is expected to substitutionally replace Sn⁴⁺, contributing to the desired magnetic properties. X-ray diffraction (XRD) analysis of the Cr-doped SnO₂ film confirmed the growth of crystalline phases (Fig. 1e). Crucially, post-annealing XRD patterns of the heterostructured films exhibited strong characteristic peaks corresponding to the (200), (210), (221), and (212) planes of Ti_{0.6}Sn_{0.4}O₂ (PDF CARD No.: 01-070-4406), confirming the successful development of Ti_{0.6}Sn_{0.4}O₂ film^{15,23,24} (Fig. 1f). The formation of Ti_{0.6}Sn_{0.4}O₂ is facilitated by the similar ionic radii of Ti⁴⁺ (0.605 Å) and Sn⁴⁺ (0.69 Å), allowing for the formation of a solid solution over a wide compositional range.^{24–26} In our Ti_{0.6}Sn_{0.4}O₂ film, Sn⁴⁺ ions substitutionally replace Ti⁴⁺ ions, with approximately 40% of

the Ti sites occupied by Sn. Furthermore, the peaks associated with (101) and (301) of anatase TiO₂ were also observed (Supplementary Note 1 and Fig. S3, ESI†).

The magnetic properties of the multiferroic films were characterized at room temperature using an out-of-plane external magnetic field, with results compared to those of non-doped SnO₂ films.²⁷ At zero magnetic field, the remanent magnetization was approximately 40% of the saturation magnetization (Fig. 1g), indicating a notable ferromagnetic response. The magnetic field-dependent magnetization curves (Fig. 1h) exhibited consistent behavior and remanent magnetization relative to the saturation level, suggesting the multi-domain nature of the Cr-doped SnO₂ layer.

The piezoelectric responses of the multiferroic films were evaluated using piezoelectric force microscopy (PFM). The amplitude–voltage curve and butterfly loops reflect the magnitude of the local piezoelectric response.²⁸ The observations revealed a clear 180° phase difference (hysteresis loop in Fig. 1i), a butterfly-shaped piezoresponse amplitude (Fig. 1j), and a pronounced hysteresis loop in the polarization *vs.* V_G graph. Furthermore, phase-voltage, amplitude–voltage, and polarization *vs.* hysteresis loops were systematically measured over 100 consecutive switching cycles. The results exhibit meaningful reproducibility, confirming the absence of fatigue degradation in the ferroelectric domains (Fig. S4–S6, ESI†). These features confirm the ferroelectric/piezoelectric characteristics of the complex metal oxide structure. Since the V_G bias was applied to the Ti_{0.6}Sn_{0.4}O₂ film, we attribute the observed ferroelectric characteristics and of this layer. Stannous titanate (SnTiO₃) is known to possess a distorted perovskite structure (orthorhombic, *Pnma* space group)^{24,29} driven by the off-centering of Sn²⁺ and Ti⁴⁺ ions, yielding a predicted spontaneous polarization (P_s) of approximately P_s ≈ 35–45 μC cm⁻² along the *b*-axis.^{30–32} In contrast, the Ti_{0.6}Sn_{0.4}O₂ film in this study adopts a distorted rutile structure, deviating from the traditional perovskite (ABO₃) arrangement. Although the ideal rutile structure of Ti_{0.6}Sn_{0.4}O₂ is not expected to exhibit ferroelectricity, the impaired network created by octahedral tilting and cation substitutions generates dipoles. The cooperative alignment of these dipoles results in macroscopic polarization. Consequently, the strain-induced coupling between TiO₆ and SnO₆ octahedra enhances the piezoelectric response of the film. Notably, our multiferroic film exhibited a P_s of 9.0 μC cm⁻² at an electric field of 10 kV cm⁻¹ (Fig. 1k). This reduced value is attributed to the lower Sn content and the different crystal structures (rutile-derived *vs.* perovskite), and also the magnitude of the field intensity. We therefore conclude that the ferroelectricity in our film originates from a combination of factors: (i) cation disorder (Sn⁴⁺ substitution in TiO₂), (ii) lone-pair effects (inherited from SnTiO₃-like behavior), and (iii) structural distortions (octahedral tilting and cation off-centering). Specifically, pristine PFM amplitude images of the nanostructures exhibiting upward topological features (Fig. 1l, PFM amplitude map) revealed bright, narrow patterns. Upon reversing the scanning bias voltage to ±10.0 V, these bright patterns transitioned to dark regions at corresponding



locations, confirming the vertical polarization component switching of the ferroelectric domains. Concurrently, the PFM phase reversibly switched between up-convergent and down-convergent textures upon application of opposite tip bias voltages. These voltage-stimulated switchable topological nano-patterns are consistent with the fundamental ferroelectric characteristics of the developed nanostructures.

Microstructural and electronic characteristics

A typical high-resolution transmission electron microscopy (HR-TEM) cross-sectional image (Fig. 2a and Fig. S7, ESI[†]) depicts an epitaxial transition at the heterointerfaces. The corresponding FFT (Fig. 2b) and SAED patterns show the

characteristics of the (200), (210), (221) and (211) crystalline planes of $\text{Ti}_{0.6}\text{Sn}_{0.4}\text{O}_2$ ²³ correspond to the previously observed XRD patterns of the multiferroic films (Fig. 1f). Supplementary Note 2 and Note 3 and Fig. S7–S10 (ESI[†]) represent the microstructural characteristics of the multiferroic film. A typical HR-TEM image of the buffer zone of approximately 2.0–4.0 nm shows crystalline structures (Fig. 2c), corresponding to the $\text{Ti}_{0.6}\text{Sn}_{0.4}\text{O}_2$ phase. Atomically resolved EDS line scans across the 4.0 nm length of heterointerfaces (Fig. 2c and Fig. S10, ESI[†]) show the decline of elemental Sn intensity to approximately one-third of the initial values across the 4.0 nm scan lines from the SnO_2 layer towards the TiO_2 film, while the intensity of elemental Ti enhanced twice, confirming the stable presence

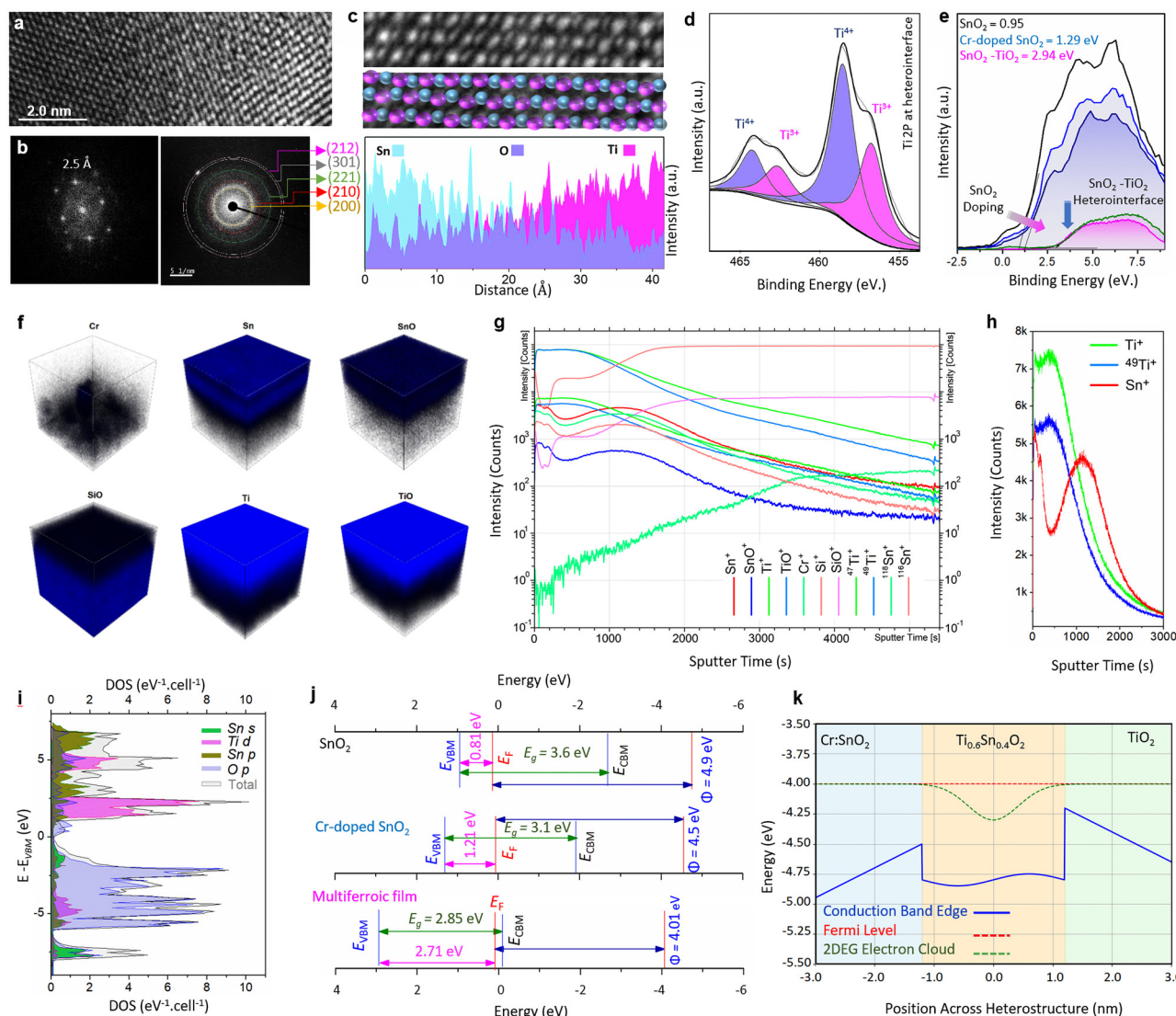


Fig. 2 Microstructural and electronic analysis of the complex metal oxide heterointerface. (a) High-angle annular dark-field scanning transmission electron microscopy (HAADF-STEM) image of the multiferroic heterojunction. (b) The corresponding FFT and SAED patterns. (c) HRTEM image and its corresponding atomic-resolution EDS line scan providing quantitative elemental information across the heterointerface. (d) The Ti 2p XPS spectra at heterointerfaces. (e) The VBM of the deposited thin films. (f) Three-dimensional (3D) time-of-flight secondary ion mass spectrometry (TOF-SIMS) map and (g) line profile showing the distribution of elemental and ionic species across the heterointerface. (h) The detailed TOF-SIMS intensity of the Ti^+ , $^{49}\text{Ti}^+$ and Sn^+ of the complex metal oxide film. (i) The calculated density of states for the $\text{Ti}_{0.6}\text{Sn}_{0.4}\text{O}_2$ complex metal oxide film. (j) The band energy alignment of the developed heterointerfaces. (k) Schematic energy band diagram illustrating the formation of a quantum well and 2DEG at the Cr-doped $\text{SnO}_2/\text{Ti}_{0.6}\text{Sn}_{0.4}\text{O}_2/\text{TiO}_2$ heterointerface.



and higher content of elemental Ti atoms at the interdiffusion layer. Moreover, the intensity of elemental O remains constant along the 4.0 nm length heterointerfaces.

XPS analysis of the Ti 2p core level reveals a mixed-valence state, with Ti^{3+} and Ti^{4+} peaks in a 3 : 4 area ratio (Fig. 2d). This corresponds to an average Ti oxidation state of +3.57, indicating 43% of Ti ions reside in the intermixed region. The emergence of Ti^{3+} stems from electronic reconstruction driven by lattice distortions, oxygen vacancies, and Sn/Ti electronegativity mismatch.³³ The resulting graded heterointerface features a distorted structure with modified Sn–O and Ti–O bonds. This interfacial reconfiguration modulates the electronic properties, highlighting its potential for tailoring the functionality of oxide heterostructures.³³ XPS depth profiling across the heterointerface revealed a dramatic valence band maximum (VBM) realignment, a hallmark of electronic reconstruction critical for emergent interfacial phenomena. Pristine SnO_2 exhibited a VBM of 1.04 eV, which modestly increased to 1.25 eV upon Cr-doping (Fig. 2e), consistent with Cr 3d orbital hybridization near the Fermi level. The pivotal observation, however, emerged upon TiO_2 deposition: the VBM abruptly surged to 2.94 eV (Fig. 2e), a 135% enhancement relative to Cr-doped SnO_2 . This colossal VBM offset (~ 1.7 eV) directly correlates with the formation of the $\text{Ti}_{0.6}\text{Sn}_{0.4}\text{O}_2$ solid solution, as Sn and Ti cations intermix. Critically, this valence band bending is the mirror image of an equally dramatic conduction band offset ($\Delta E_c \approx 0.5\text{--}1.0$ eV), driven by the electron affinity mismatch between SnO_2 ($x \approx 4.5$ eV) and TiO_2 ($y \approx 5.1$ eV). Electrons from SnO_2 are thus compelled to spill over into the TiO_2 -derived conduction band states, accumulating in a quantum well formed at the heterointerface. This charge transfer, coupled with quantum confinement perpendicular to the interface, sets the stage for the formation of a 2DEG.^{34,35} The $\text{Ti}_{0.6}\text{Sn}_{0.4}\text{O}_2$ intermixed phase mitigates lattice mismatch and reduces interfacial disorder, preserving coherent d-orbital overlap essential for high-mobility electron transport.

Time-of-flight secondary ion mass spectrometry (TOF-SIMS) of the heterointerfaces (Fig. 2f) revealed a non-monotonic depth profile of Sn and Ti ions. Notably, Ti^+ and TiO^+ intensities exhibited an S-shaped decline from the upper surface towards the heterointerface, whereas Sn^+ and SnO^+ signals displayed a bimodal distribution: high at the surface, depleted in the middle of the heterostructured layer, and re-intensified near the SnO_2 sublayer (Fig. 2g and h). We attribute the anomalous Sn distribution to oxygen vacancy-mediated diffusion under reducing thermal annealing. The forming atmosphere partially reduces TiO_2 , generating V_{O} that facilitate $\text{Sn}(\text{iv}) \rightarrow \text{Sn}(\text{ii})$ conversion and enhance interstitial migration.^{36,37} The surface acts as a sink for Sn due to lowered surface energy (Sn segregation) and re-oxidation of $\text{Sn}(\text{ii}) \rightarrow \text{Sn}(\text{iv})$, creating a chemical potential gradient that drives Sn upward diffusion.^{36,37} Diffusion activation energy of Sn^{4+} in TiO_2 is typically in the range of 2–3 eV, depending on crystal phase and defect density. However, this barrier can be significantly lower due to vacancy-mediated mechanisms. Conversely, the middle region experiences a kinetic bottleneck due to fewer V_{O} and higher Sn migration barriers (~ 2.0 eV for $\text{Sn}(\text{iv})$ vs.

~ 0.8 eV for $\text{Sn}(\text{ii})$), resulting in a depletion zone. The diffusion mechanism of Sn^+ into the TiO_2 matrix is detailed in Supplementary Note 4 (ESI†). A model illustrating non-equilibrium Sn diffusion within SnO_2 – TiO_2 heterointerfaces is presented in Supplementary Note 5 (ESI†).

The electronic density of states (DOS) for the crystalline $\text{Ti}_{0.6}\text{Sn}_{0.4}\text{O}_2$ structure, calculated *via* a hybrid functional DFT approach, is presented in Fig. 2i (Supplementary Note 6, ESI†). The conduction band maximum (CBM) is primarily composed of Ti 3d states, consistent with a TiO_2 electronic structure. In the valence region, the oxygen 2p orbitals dominate the lower bands, while a set of broad features overlapping and extending above the O 2p manifold arises due to hybridization with Sn 5s and, to a lesser extent, Sn 5p orbitals. This hybridization results in a pair of bands straddling the O 2p peak – a signature consistent with the revised lone pair model proposed by Walsh *et al.*,³⁸ where the Sn 5s–O 2p–Sn 5p interactions give rise to antibonding states near the VBM. The upper of these hybridized bands exhibits an antibonding character and contributes significantly to the VBM. The localization and energetic positioning of these states suggest an electrochemically active lone pair on $\text{Sn}(\text{ii})$,³⁹ leading to a ~ 4.0 eV modulation in the ionization potential – a trend also observed in related $\text{Sn}(\text{ii})$ -based oxides.³⁹ The observed VBM dispersion also supports the presence of directional Sn–O orbital overlap and potential delocalization pathways. The incorporation of Cr^{3+} ions, which substitute for Sn^{4+} in rutile SnO_2 , creates localized states within the bandgap, as evidenced by in the electronic DOS.⁴⁰ The charge compensation mechanisms are induced due to partial substitution, possibly involving O_v , which can enhance carrier concentration and influence magnetic ordering. The Cr 3d states hybridize with O 2p orbitals, contributing to the valence band edge and slightly narrowing the bandgap of SnO_2 .⁴⁰ Structural integrity of the SnO_2 rutile phase is preserved, as confirmed by XRD, though minor peak shifts suggest lattice distortion due to ionic radius mismatch between Cr^{3+} and Sn^{4+} . Furthermore, the Cr doping induces a shift in the Fermi level towards the conduction band, indicating an increase in the electron carrier concentration. Furthermore, the heterostructured multiferroic films exhibit clear n-type semiconducting behavior, as evidenced by a significant upward shift of the Fermi level toward the conduction band edge following the formation of the intermediate $\text{Ti}_{0.6}\text{Sn}_{0.4}\text{O}_2$ phase. This shift is attributed to the combined effects of a reduced bandgap of the heterostructure, measured at approximately 2.8 eV, and the Burstein–Moss effect,⁴¹ wherein increased carrier concentration leads to the Fermi level entering the conduction band. Additionally, the observed reduction in work function to 4.01 eV further supports the modified electronic structure and enhanced electron affinity of the film. These results suggest a tailored band alignment and carrier distribution within the heterostructure. The valence band maximum (VBM) is dominated by O 2p orbitals hybridized with Sn 5s and 5p states, resulting in an antibonding character at the top of the valence band, in agreement with the revised lone pair model proposed for $\text{Sn}(\text{ii})$ -based oxides. This band configuration promotes the



formation of 2DEG at the $\text{SnO}_2/\text{Ti}_{0.6}\text{Sn}_{0.4}\text{O}_2$ interface, where transferred electrons are confined within the well due to favorable conduction band offsets. Fig. 2j provides crucial insights into the energy level alignment of the developed thin films, driven from bandgap determination, VBM measurements and work function analysis using Kelvin probe force microscopy (KPFM) (Fig. S11, ESI[†]). Notably, the measured work function of the multiferroic heterostructure was lower than that of both pristine and Cr-doped SnO_2 . Furthermore, the multiferroic film exhibited a slightly reduced bandgap of 2.85 eV compared to the Cr-doped SnO_2 film. The observed n-type behavior of the multiferroic heterointerfaces can be attributed to the Fermi level shift towards the conduction band edge upon Sn/Ti incorporation within the interfaces. The decrease in work function from 4.5 eV in Cr-doped SnO_2 to 4.01 eV in the multiferroic film suggests an increased carrier concentration resulting from the substantial doping.⁴²

The formation of the 2DEG at the Cr-doped $\text{SnO}_2/\text{Ti}_{0.6}\text{Sn}_{0.4}\text{O}_2/\text{TiO}_2$ heterointerface can be understood through the band alignment and quantum well formation facilitated by the intermediate $\text{Ti}_{0.6}\text{Sn}_{0.4}\text{O}_2$ layer (Fig. 2k and Supplementary Note 7, ESI[†]). Based on hybrid functional DFT-calculated band gaps and

reported work functions, Cr-doped SnO_2 and TiO_2 exhibit conduction band minima (CBMs) at higher energies relative to $\text{Ti}_{0.6}\text{Sn}_{0.4}\text{O}_2$. This band offset leads to the formation of a type-I quantum well,⁴³ where the $\text{Ti}_{0.6}\text{Sn}_{0.4}\text{O}_2$ layer acts as a potential well for electrons. Upon contact, Fermi level equilibration results in electron transfer from both Cr-doped SnO_2 and TiO_2 into the lower-energy conduction band of $\text{Ti}_{0.6}\text{Sn}_{0.4}\text{O}_2$. The resulting accumulation and confinement of electrons within this narrow region give rise to a 2DEG, where carriers are free to move in the in-plane directions but are quantum-confined in the out-of-plane direction. This confinement is enhanced by the high dielectric constants and favorable effective masses of the constituent oxides. The model suggests that the 2DEG is localized within a few nanometers of the $\text{Ti}_{0.6}\text{Sn}_{0.4}\text{O}_2$ layer, forming a highly conductive interfacial channel that may be exploited in oxide-based electronic and spintronic devices.

Ferroelectric and topological switching characteristics

The structural transformation observed in the AFM and KPFM analysis (Fig. 3a)—specifically, the emergence of vertically oriented, planar crystalline features—suggests significant

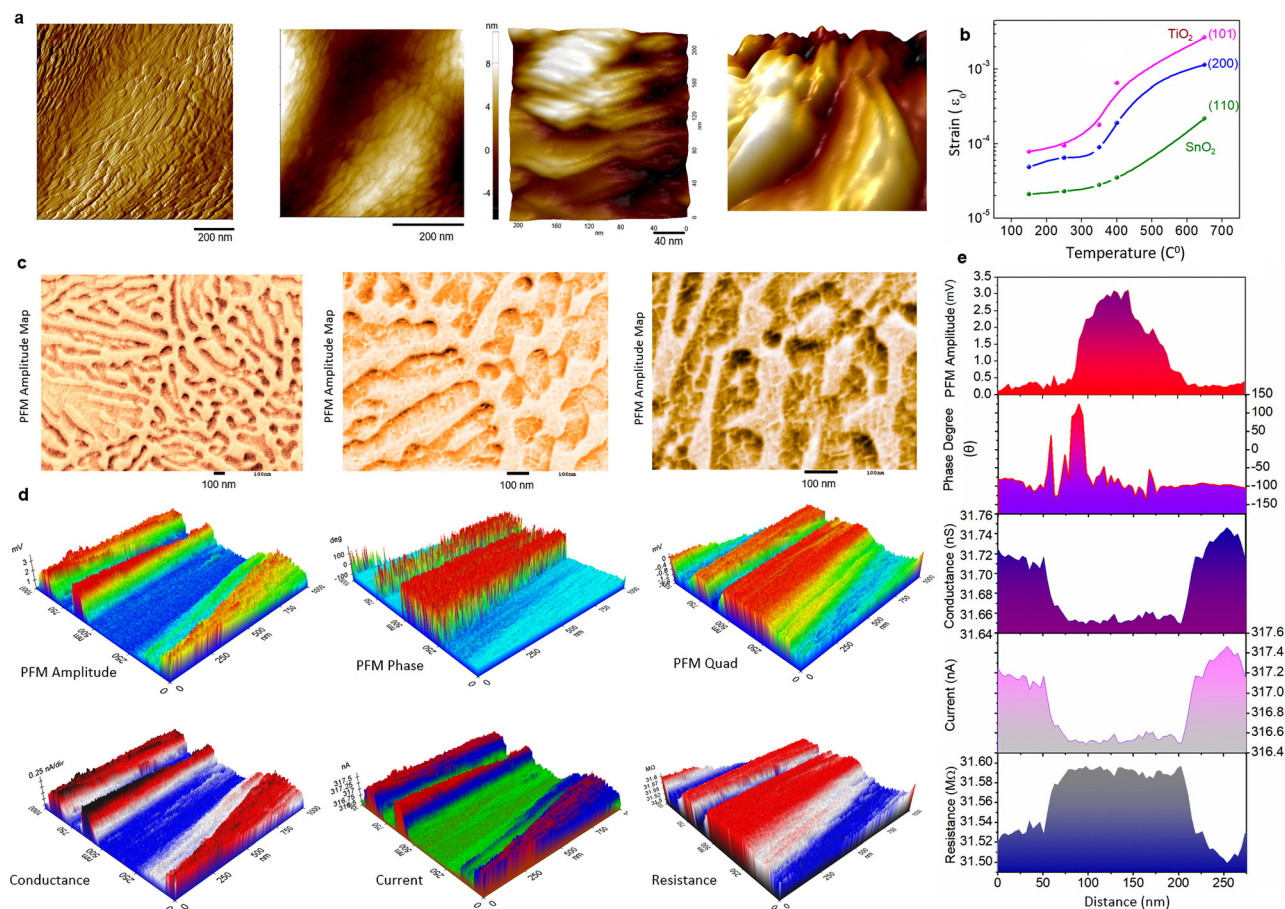


Fig. 3 Surface morphology and 3D PFM image of the complex heterostructure. (a) AFM & KPFM topography image showing the overall surface morphology of the metal oxide heterointerface. (b) The effect of thermal annealing on the induced strain to the heterostructured films. (c) Piezoresponse force microscopy map image (PFM), depicting the piezoresponse amplitude of the polarized domains. (d) The 3D PFM amplitude map, phase image and phase quad showing the vertical polarization in the forward bias state, accompanied by (bottom row) the 3D map of conductance, the current and resistance of the polarized domains. And corresponding (e) statistical data of the polarized domains.



reorganization at the surface of the multiferroic film after thermal annealing. Atomic force microscopy (AFM) analyses demonstrated that the planar crystalline plane exhibited an average surface roughness of 1.169 nm (Fig. S12 and S13, ESI†). The detailed results on the roughness measurements of the film are presented in Table S1 (ESI†). The surface morphology of multiferroic film and its morphological evolution is accompanied by the calculated lattice strain, as quantified by XRD analysis at different annealing temperatures (Fig. 3b). The (110) plane of SnO₂ exhibited a modest but consistent increase in strain from 0.002% at 150 °C to 0.022% at 650 °C. In contrast, the TiO₂ component displayed more substantial strain development: the (200) plane of TiO₂ showed strain increasing from 0.0047% to 0.11%, while the (101) plane of TiO₂ exhibited the highest strain evolution, rising from 0.0081% to 0.26% across the studied temperature range. Although these values are relatively moderate compared to those reported in some literature – *i.e.* 0.5% to 2.5% b strain in TiO₂ thin films⁴⁴ – and 1.3% to 4.5% in SnO₂ films⁴⁵ – they remain within the lower bound of what is typically reported for polycrystalline metal oxide films. A comprehensive review on strain in metal oxide thin films has noted a broader range from 0.1% to 10.0%, depending on the material system, deposition method, and post-deposition treatments.⁴⁶ The relatively lower strain values in our system may be attributed to the partial relaxation of interfacial stress due to the formation of ultra-thin (≤ 10.0 nm) planar crystalline layers. The role of strain in enhancing the piezoresponse of multiferroic film is well-established,⁴⁷ and the observed strain-induced modifications here provide a solid foundation for understanding the piezoelectric response of the multiferroic system. PFM mapping of the surface of the multiferroic film typically reveals a uniform distribution of polarized domains across the surface (Fig. 3c). These ferroelectric nanodomains exhibit lateral and cross-sectional dimensions on the order of hundreds of nanometers. Subsequent PFM measurements of the domains corroborated the observation of phase changes and PFM amplitude alterations (Fig. 3d and e), confirming the ferroelectric–piezoelectric nature of the multiferroic film. Overlays of PFM amplitude and phase maps, corresponding to the forward vertical polarization (0° head rotation angle) at a tip bias of 0 V and a sample bias of 10.0 V, on the 3D topography are shown in Fig. 3d. The spatial distribution of vertical polarization within the patterned regions, reflecting local electric field domains (Fig. 3d). Similarly, downward polarization exhibited analogous patterns and configurations. Notably, the ferroelectric patterns displayed significant contractions in both upward and downward modes, confirming the switchable polarization characteristics of the fabricated multiferroic film. The application of a DC bias voltage to the ferroelectric domains induced an electrical driving force. Subsequent measurements of vertical polarization amplitude and phase under positive and negative DC bias voltages demonstrated the switchable polarization behavior of the nanostructures. Additionally, conductive atomic force microscopy (c-AFM) investigation indicated a slight decrease in conductance in non-polarized regions (Fig. 3d down panel, and Fig. 3e), while piezoelectric domains exhibited higher

conductance (Fig. S14, ESI†). Vertical PFM measurements confirm the presence of switchable polarization, suggesting an intrinsic ferroelectric order conducive to domain switching.⁴⁸ The ferroelectricity observed in the multiferroic film likely arises from a complex interplay of the material's composition, structural characteristics, defect chemistry, and thermal treatment. The substitution of Sn into the TiO₂ lattice in the ALD process and the formation of Ti_{0.6}Sn_{0.4}O₂ structures can induce ferroelectric properties by creating lattice distortions, modifying the electronic band structure, and introducing local structural asymmetries that support spontaneous polarization. The alignment of ferroelectric polarization along the *c*-axis of the planar nanostructures further suggest a geometric dependence of ferroelectricity,⁴⁹ as observed in the formation of switchable 2DEGs based on the ferroelectric⁴⁹ Ca:SrTiO₃. The increased conductivity within piezoelectric domains suggests an interplay between ferroelectric–piezoelectric state and local electronic transport, influencing the formation of anticipated type I 2DEG at the interface. Understanding this relationship is crucial as we proceed to the direct measurements of the characteristics of the 2DEG layer in the subsequent section.

Characteristic of the multiferroic 2DEGs

Fig. 4a depicts the variation of mobility of the heterostructured multiferroic film at various temperatures. The measurements showed that the carriers at metal oxide heterointerfaces are electron type (n-type). The electro mobility (μ_e) increased by the cooling of the sample, and it is around $1.734 \times 10^3 \text{ cm}^2 \text{ V}^{-1} \text{ s}^{-1}$ at 7.0 K, while it decreases to $\sim 10^2 \text{ cm}^2 \text{ V}^{-1} \text{ s}^{-1}$ at room temperature. This typical behavior was also observed in the study of the temperature-dependent mobility of SrTiO₃ heterostructures,⁵⁰ where the electron mobility increases upon cooling rate and reached to vicinity of $200 \text{ cm}^2 \text{ V}^{-1} \text{ s}^{-1}$ at 2.0 K.⁵⁰ The sheet resistance also follows temperature-dependent changes, where an evident metallic to insulator transition behavior is observed upon increasing the measurement's temperature (Fig. 4b). The sheet resistance of the heterostructure experienced a sharp and consistent decline between the room temperature to 100 K, and then remained almost constant up to 7.0 K. The typical sheet resistance of the heterostructure is $1.8 \times 10^4 \Omega$, while it reached to 104.7Ω at 7.0 K. This transition indicates the development of 2DEG in this system.^{51,52} The room temperature sheet resistance of our heterostructure is quite close to the previously reported sheet resistance values for the formation of 2DEG at Al₂O₃/TiO₂ heterointerfaces ($1.8 \times 10^4 \Omega \text{ sq}^{-1}$),⁵¹ and $10 \text{ k}\Omega \text{ sq}^{-1}$ for yttria stabilized zirconia⁵³ (YSZ)/SrTiO₃ (STO), $\sim 17.5 \text{ k}\Omega \text{ sq}^{-1}$ for STO/STO,⁵³ 10^3 – $10^4 \Omega \text{ sq}^{-1}$ in Al₂O₃/In₂O₃⁵⁴ and $2.4 \times 10^4 \text{ } 10^3 \Omega \text{ sq}^{-1}$ for BeO/ZnO metal oxide heterostructures.⁵⁵ The temperature dependence of sheet concentration is also depicted in Fig. 4b. The obtained sheet carrier density declined gradually upon cooling from room temperature to 100 K, while the rate of decrement of the sheet carrier did not alter considerably upon cooling further than 100 K, where the maximum values of sheet concentration was $\sim 3.4 \times 10^{12} \text{ cm}^{-2}$. The sheet carrier density of the present multiferroic films are comparable to the previously reported values for the formation of 2DEGs⁵³ at STO/STO



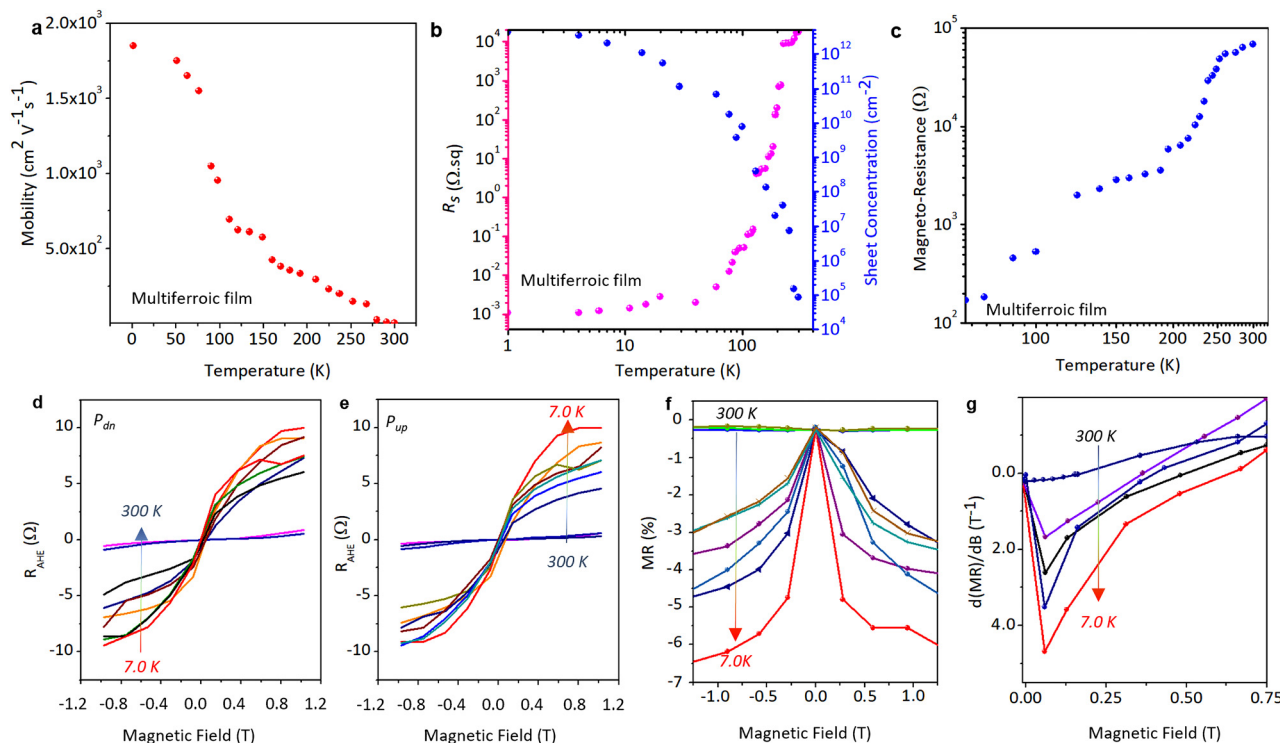


Fig. 4 The temperature dependence (a) Hall mobility (μ_{Hall}), (b) sheet resistance (R_s), sheet concentration, and (c) magneto-resistance of the heterostructured complex oxide film. The magneto-transport characteristics of the Multiferroic 2DEGs. (d) The temperature dependence AHE resistance at upward and (e) downward polarization at different temperatures. (f) The MR and its (g) corresponding magnetic field derivative of the 2D electron gas at different temperature and magnetic field for upward polarization.

($\sim 8.0 \times 10^{13} \text{ cm}^{-2}$), YSZ/STO ($\sim 7.0 \times 10^{12} \text{ cm}^{-2}$), LAO/STO ($12.0 \times 10^{13} \text{ cm}^{-2}$), 10^{13} – 10^{14} cm^{-2} in $\text{Al}_2\text{O}_3/\text{In}_2\text{O}_3$ heterostructure,⁵⁴ 10^{14} cm^{-2} in BeO/ZnO and $1.0 \times 10^{12} \text{ cm}^{-2}$ in $\text{LaAlO}_3/\text{EuTiO}_3/\text{Ca-SrTiO}_3$ heterostructures.⁵⁶ In our system, the observed smooth heterointerface transition excludes the polar catastrophe as the origin of the 2DEG. Instead, oxygen vacancy formation is indicated as the most likely cause, supported by the observation of Ti^{3+} at the heterointerfaces (Fig. 2d).

The significant increase in magnetoresistance (MR) from $1.1 \times 10^2 \Omega$ at 7.0 K to $10^5 \Omega$ at room temperature in the multiferroic Cr-doped $\text{SnO}_2/\text{Ti}_{0.6}\text{Sn}_{0.4}\text{O}_2/\text{TiO}_2$ heterostructure suggests a substantial enhancement of the spin-dependent transport properties (Fig. 4c). This enhancement is attributed to the increased thermal energy, which may lead to a more efficient spin injection and detection, as well as a modification of 2DEG. The Cr doping is also believed to play a crucial role in the MR enhancement.⁵⁷ The significant increase in MR at room temperature reflects a transition toward a spin-filtered transport regime governed by polarization-controlled magnetic configurations at the interface. These findings underscore the critical role of temperature-driven multiferroic interactions in tuning magneto-transport properties and support realizing non-volatile, field-free spintronic switching functionalities in complex oxide heterostructures.⁵⁸ Therefore, we investigate the possibility of polarity-reversible, field-free switching behavior in multiferroic heterostructures. We examined the influence of current-induced spin-orbit torques on the magnetic orientation of the system.

Prior to each measurement, the samples were magnetized using an out-of-plane magnetic field of 0.5 T to define the initial magnetic state. Subsequently, 100-ms current pulses were applied along the in-plane x -direction, while varying the in-plane magnetic field between 0.2 T, 0.3 T, 0.5 T, and 0.7 T to assist the switching process. The Hall resistance (R_H) was measured after each current pulse to monitor changes in the magnetization state and to detect switching behavior. The representative R_H - I curves and corresponding switching loops, shown in Fig. S15 and S16 (ESI[†]), exhibit polarity-dependent characteristics, influenced by the magnitude of the magnetic field and also the applied electric field.

To explore the spin-dependent transport properties of the heterostructures, the anomalous Hall effect (AHE) was investigated under upward and downward polarization states (P_{up} & P_{dn}) across a temperature range of 7.0 K to 300 K. Fig. 4d and e present the temperature-dependent evolution of the AHE component under an applied out-of-plane magnetic field. The measurements reveal a clear trend of gradual suppression of the AHE signal with increasing temperature. While the anomalous Hall resistance decreases continuously from 7.0 K to 300 K, it does not vanish entirely at any measured temperature, indicating that spin-polarized transport persists across the full thermal range studied. The observed decline in AHE magnitude with temperature is consistent with the expected reduction in spin polarization and magnetic ordering due to thermal fluctuations. Although the resistance does not reach zero within the experimental window, the extrapolated trend suggests the



potential for AHE resistance to approach zero at temperatures near absolute zero.⁵⁹ This behavior draws an interesting parallel to the quantum Hall Effect (QHE), a phenomenon characterized by vanishing longitudinal resistance under strong magnetic fields at cryogenic temperatures (typically below 4.0 K). While the QHE is not observed here, the declining AHE response reinforces the notion that quantum transport regimes may emerge in this system under more extreme cooling conditions.

To study the magneto-transport behavior of films, Hall MR measurements were performed across a temperature range of 7.0 K to 300 K under both upward and downward polarization states. The measurements were conducted by sweeping the magnetic field symmetrically from $-1.0 T$ to $+1.0 T$. In both polarization conditions, the anomalous Hall resistance exhibited a distinct ring-bell-shaped dependence on the magnetic field: the MR % was approximately 0% at zero magnetic field and decreased symmetrically to a minimum of about -7.0% at both $+1.0 T$ and $-1.0 T$ at 7.0 K (Fig. 4f). As the temperature increased, the MR% gradually diminished, reaching approximately -3% at 300 K, while maintaining the same overall shape. The observed negative magnetoresistance (MR) in our multiferroic heterostructures deviates from the positive MR typically observed in many non-magnetic materials, which commonly arises from classical Lorentz force effects or quantum weak localization⁶⁰ (WL). While WL can indeed induce negative MR in disordered non-magnetic systems as demonstrated in previous studies on un-doped SnO₂ films,⁶⁰ the behavior observed in the anomalous Hall configuration is primarily attributed to spin-dependent scattering mechanisms,⁶¹ which are significantly influenced by the presence of localized magnetic moments introduced by Cr doping. In this ferromagnetic layer, the inherent disorder of these localized magnetic moments acts as a significant scattering source for conduction electrons. At low temperatures, these magnetic moments are more easily aligned by the external magnetic field, leading to a suppression of spin-disorder scattering and a corresponding enhancement of negative MR. As temperature increases, thermal agitation disrupts magnetic alignment, reducing the effectiveness of the magnetic field in suppressing scattering and thereby decreasing the magnitude of MR. The negative field dependence of the MR at lower temperatures is a clear indication of some degree of spin disorder in magnetic systems.⁵⁶ Furthermore, if spin-polarized interfacial scattering or tunneling MR effects are present at the Cr-doped SnO₂/Ti_{0.6}Sn_{0.4}O₂ interface, these mechanisms could also contribute to the negative MR by facilitating more efficient spin-aligned conduction paths under a magnetic field.⁶⁰ Therefore, the negative MR in our system serves as a characteristic signature of its magnetic properties and the suppression of spin-disorder scattering. Additionally, the anomalous Hall measurement geometry—likely sensitive to interfacial, spin-related, and anisotropic transport phenomena—may amplify these effects relative to the conventional Hall configuration, which is more reflective of bulk transport properties. The derivatives of the MR vs. the variation of external magnetic field (Fig. 4g) represents an inflection signals, evidenced at lower measurement temperatures at a pronounced magnetic field of

$\sim 0.07 T$. This inflection was attributed to the occurrence of saturation of the magnetic lattice of the structures.⁵⁶ These results collectively suggest that the MR in the anomalous Hall configuration is governed by a complex interplay of magnetic scattering, interfacial conduction paths, and polarization-dependent effects, which are highly sensitive to both temperature and magnetic field strength.

To understand the origin of the observed magnetoresistance we combined theoretical modeling and practical measurements (detailed in Supplementary Note 8, ESI†). Two sets of thickness-dependent experiments were conducted at 7.0 K. In the first set, with a constant 5 nm thick Ti_{0.6}Sn_{0.4}O₂ ferroelectric layer, varying the Cr-doped SnO₂ ferromagnetic layer's thickness from 0 to 50 nm showed a sharp decrease in MR % from near 0% to a maximum negative value of approximately -7.0% at 10 nm thick Cr-doped SnO₂ (Fig. S17a, ESI†). Further increasing the Cr-doped SnO₂ thickness (10 nm to 50 nm) resulted in the MR % gradually saturating and recovering to about -5.5% . This behavior suggests the -7% peak MR is primarily interface-driven, enhanced by efficient interfacial phenomena like spin-dependent scattering or magnetoelectric coupling,^{60,61} which are most prominent when the interface-to-volume ratio is maximized. The subsequent slight recovery indicates a dilution of this strong interfacial contribution by the increasing bulk volume.^{60,61} These observations are in good agreement with our predicted model (Fig. S17b, ESI†), which incorporates a combined mechanism of interface and bulk contributions to understand the multiferroic films' magnetoresistance behavior. This model specifically predicted the dominance of the interface effect when the thickness is less than or close to 10 nm. Further supporting this dominant interfacial role, practical results (Fig. S18, ESI†) from a second set of experiments investigating the Ti_{0.6}Sn_{0.4}O₂ thickness were obtained. With a constant 10 nm Cr-doped SnO₂, the MR at 7.0 K initially decreased to -7% at ~ 5 nm Ti_{0.6}Sn_{0.4}O₂ (likely its critical ferroelectric thickness), then remained remarkably constant up to 50 nm. This insensitivity to the bulk ferroelectric thickness confirms its primary contribution is interfacial, enabling stable, robust magnetoelectric coupling, rather than being a volume-dependent effect. Collectively, these findings demonstrate that while bulk ferromagnetic Cr-doped SnO₂ provides fundamental magnetic properties, the enhanced MR response is predominantly governed by intricate interactions and spin-dependent phenomena occurring at the SnO₂-Ti_{0.6}Sn_{0.4}O₂ multiferroic heterointerface.

To investigate the interplay between quantum transport ferroelectricity and ferromagnetism, magnetotransport measurements were conducted under varying gate conditions. Both longitudinal resistance (R_{xx}) and Hall resistance (R_{xy}) were measured simultaneously while subjecting the samples to pulsed magnetic fields up to $2.0 T$ at 7.0 K (Fig. S19a and b, ESI†). To probe the gate-dependent response, a series of back-gate voltages (V_g) ranging from 1.0 to 10.0 V were applied at the rear face of the substrate, effectively modulating the carrier density and polarization state of the 2DEG. As V_g increased, gate-induced depopulation of the 2DEG led to a pronounced rise



in zero-field resistance and a concomitant enhancement indicative of suppressed screening and increased electron–electron interactions at lower carrier densities. Such behavior is consistent with a reduction in mobile carrier density and enhanced scattering, likely influenced by both the presence of magnetic nanodomains and controlled ferroelectric polarization.⁶² Remarkably, while (R_{xy}) (Fig. S19b, ESI†) exhibited linear field dependence at all temperatures (classical Hall-Effect), Shubnikov–de Haas (SdH) oscillations^{63,64} emerged in (R_{xy}) below 10.0 K and above 15 T (Fig. S19c, ESI†). These quantum oscillations confirm the coexistence of multiferroic order and quantum transport phenomena in these heterostructures (Supplementary Note 9, ESI†).

Multiferroic FET-artificial synaptic junctions

The complex logic functions of ferroelectric memristors have been previously characterized. The ferroelectric field-effect transistors (FeFETs) exhibit great versatility with rich dynamics,

making it suitable for both memory arrays and synaptic circuits.^{65–67} Our FET device (Fig. 5a) integrates a multiferroic film as the core synaptic junction, positioned between adjacent source and drain electrodes on a SiO₂–Si substrate. This specific design includes four source/drain electrodes, allowing for facile and versatile electrical measurements (Fig. S20, ESI†). An upper Pt gate electrode is crucial for modulating the synaptic weight, controlling the electrical connection between the source and drain. The heterostructured material arrangement at this gated-synaptic junction is distinctly visible in the cross-sectional TEM image (Fig. 5b). To confirm the performance of our multiferroic films in FET architecture, Fig. 5c showcases consistent current–voltage (I – V) responses with ultra-low read currents across four separate devices at $V_G = 0$ V. Fig. S20 (ESI†) provides additional details on the FET device.

We also investigated the cyclic I – V memristive characteristics of the FET device. Significantly, a vivid transition from

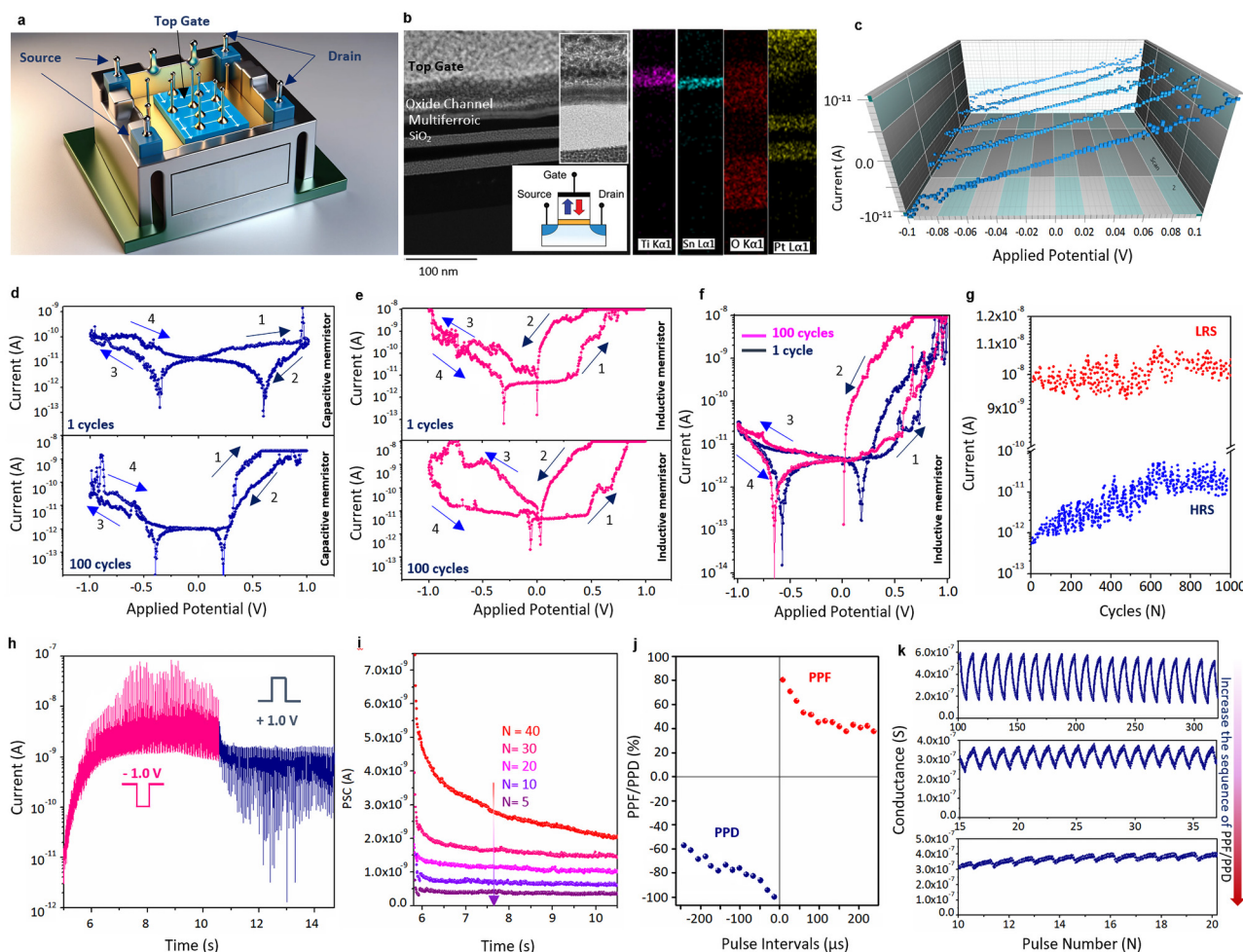


Fig. 5 (a) Schematic diagram of the 3-terminal FET device where the gate and drain electrodes are used as the pre- and post-synaptic terminals, (b) cross-sectional HR-TEM with STEM-EDS maps confirming the SnO₂/Ti_{0.6}Sn_{0.4}O₂/TiO₂ stack. (c) The typical I – V curves of the heterojunctions. (d) Capacitive switching in a Pt/SnO₂–TiO₂/Pt memristor junction. (e) Inductive switching in Pt/Cr–SnO₂/Ti_{0.6}Sn_{0.4}O₂/TiO₂/Pt. (f) Inductive switching in Au/Cr–SnO₂/Ti_{0.6}Sn_{0.4}O₂/TiO₂/Pt. (g) Endurance of HRS and LRS over 10³ cycles. (h) Potentiation and depression under ± 1 V, 100 Hz pulses. (i) Spike-rate-dependent depression of synaptic conductance. (j) PPF/PPD characteristics for a FE-FET synapse by measuring the synaptic strength change as a function of the pulse interval, showing a biological synapse behavior. (k) The variation of synapse channel conductance of the synaptic junctions at various sequences of the measurements of the PPF/PPD sequences.



capacitive to inductive behavior was observed when comparing the Pt/SnO₂-TiO₂/Pt junction to the Pt/Cr-SnO₂/Ti_{0.6}Sn_{0.4}O₂/TiO₂/Pt device (Fig. 5d and e). This transition suggests a fundamental shift from charge storage mechanisms, where capacitive behavior dominates, to dynamic processes involving ionic migration, conductive filament formation, or modifications in interface properties. Such changes can lead to a phase lag in the current response, particularly relevant in the FeFET configuration.^{68–70} The observed asymmetry in *I*-*V* cyclic graphs frequently reported in ferroelectric devices, primarily arises from the formation of an internal built-in electric field. This field can originate from asymmetric interfacial chemistry (*e.g.*, defect concentrations or barrier heights), preferential charge trapping and detrapping mechanisms, or gradients in mobile ionic species such as oxygen vacancies.^{71,72}

During this transition, two notable phenomena occurred: the threshold voltages significantly decreased, and the size of the hysteresis loop, particularly its opening, became considerably larger and prominent (Fig. 5e). In ferroelectric memristors, a larger hysteresis loop directly signifies a more complete and stable ferroelectric polarization reversal, indicating that a larger portion of the ferroelectric domains are switching robustly. The conductance modulation and resulting resistive switching in these devices are intrinsically linked to this polarization state. The initial capacitive behavior reflects charge trapping and interface effects, while the subsequent inductive response points to more complex, inertia-like phenomena, potentially related to ionic or even magnetic dynamics.⁷¹ Similar capacitive-to-inductive transitions have been reported in multiferroic metal oxide films, though the current observations exhibit distinct differences, likely attributable to the coexistence and interplay of ferroelectricity and ferromagnetism.^{72,73} The observed decrease in threshold voltage primarily indicates the development of an internal bias field within the device.^{74,75} In ferroelectric materials, this internal electric field can arise from trapped charges or redistributed defects (such as oxygen vacancies),^{76,77} which bias the ferroelectric domains. This bias assists the switching process in a particular direction, effectively making it easier to switch the domains and thus reducing the required switching voltage magnitude. These combined phenomena – lower threshold voltages and larger hysteresis loops – are highly advantageous for memory and synaptic applications, as reduced threshold voltages decrease power consumption, and expanded hysteresis loops improve the distinguishability of resistive states.

In the study of the memristive behavior of the Au/Cr-doped SnO₂/Ti_{0.6}Sn_{0.4}O₂/TiO₂/Pt multiferroic films (Fig. 5f), a gradual resistive switching was observed under positive polarity, with an on/off ratio of approximately 10³. As the positive voltage scan approaches and exceeds the threshold voltage ($V_{th} \approx 0.51$ V), the current gradually increases, transitioning the device from HRS to a low resistance state (LRS) indicating the SET process. Conversely, during the reverse (negative) voltage scan, the device maintains its on state until the voltage reaches a lower threshold ($V_{th} \approx 0.24$ V), where the current decreases, switching back from LRS to HRS. The device then remains in the off

state throughout the negative polarity scan. This resistive switching exhibits volatile memory behavior. Additionally, the device has shown multistate resistive switching after sequential cyclic measurements (Fig. 5f), making it suitable for analog volatile memory applications. Fig. 5g additionally depicts the stable variation of HRS and LRS after a thousand cyclic measurements.

The voltage-dependent transient response of the multiferroic FET-synaptic junctions was investigated using a train of ± 1.0 V pulses at a frequency of 100 Hz, as depicted in Fig. 5h. By analogy, the gate terminal of the FET can be considered functionally similar to a pre-synaptic neuron, while the source-drain channel emulates a post-synaptic neuron. This structural correspondence enables the concurrent processing and transmission of signals, rendering FET a synaptic junction. The results indicate that a threshold gate voltage of -1.0 V is sufficient to induce a gradual increase in the postsynaptic current response. At lower applied voltages, the capacitive charging of the heterointerfaces manifested a sharp initial transition, which is a characteristic feature of capacitive charging processes. The device exhibited a significant inductive contribution upon applied higher voltages, which is reflected in the enhanced increment of the postsynaptic currents. When the potential pulses are discontinued, an immediate negative current response was observed which is attributed to the internal voltage and the series resistance of the device. This phenomenon is consistent with the synaptic performance reported for perovskite ceramics,⁷⁸ showing that the device mimics the dynamic and adaptive features of biological synapses. The synaptic current potentiation was also found to be dependent on the number of training voltage pulses, with increased pulses resulting in higher postsynaptic currents, thereby demonstrating the device's capacity for memory retention.

Fig. 5i illustrates the spike rate-dependent plasticity, where the device's memory retention duration extends after potentiation with varying numbers of training pulses. Notably, the gradual decline of the postsynaptic current during depression phases, stabilizing at non-zero values, reflects voltage-dependent long-term plasticity. The paired-pulse facilitation/depression (PPF and PPD) are common features for short-term synaptic plasticity (STSP) functionality of synapses. The variation of PPF and PPD *vs.* the pulse intervals time (Fig. 5j) confirms the capability of the developed FET synaptic junctions for STSP functionality. The radiation of synaptic weight confirms the exponential decay of PPF and PPD *vs.* the increase of pulse interval times. The long-term synaptic plasticity (LTSP) of the synaptic junctions was characterized by a series of repeated programming pulses, at different frequencies and the measurement sequences of PPF/PPD. Fig. 5k illustrates the conductance modulation of the FET synapse. Potentiation was induced by the application of identical negative voltage pulses (-1.0 V, 10 μ s), followed by depression using identical positive voltage pulses (1.0 V, 10 μ s). Conductance values were derived from drain current measurements performed at a drain-source bias (V_{DS}) of -0.1 V. The observed conductance variation, influenced by pulse intervals and numbers, demonstrates the long-term synaptic plasticity (LTSP) functionalities of the fabricated junctions.



63 + This trend, exhibiting an initial increase followed by a plateau in response to an increasing pulse sequence (PPFF/PPD), displays a notable dependency on pulse frequency: this behavior becomes more pronounced as frequency decreases. At its core, the FeFET modulates semiconductor channel conductance directly through the ferroelectric polarization. Applied electrical pulses reorient ferroelectric domains, thereby altering remnant polarization and electrostatically modulating the channel's carrier concentration and, consequently, its conductance.⁷⁹ This domain switching is not instantaneous; it is a kinetic process driven by domain nucleation and subsequent domain wall motion, each characterized by specific time constants.⁸⁰ At higher frequencies, the short inter-pulse intervals provide insufficient time for full, stable domain reorientation, thus limiting the effectively established remnant polarization. This results in weaker channel modulation, leading to smaller conductance increases and lower plateaus.⁸¹ Conversely, at lower frequencies, longer time intervals allow for more efficient ferroelectric domain switching, enabling a stable polarization state yielding larger conductance increases. Secondary factors including the kinetics of charge trapping/detrapping at heterointerfaces and mobile oxygen vacancy migration⁸² also contribute. Though a primary mechanism in filamentary memristors, vacancies play a significant secondary role in FeFETs. Their slow migration means higher frequencies restrict their ability to influence polarization screening or modify interface states. Conversely, lower frequencies facilitate more extensive vacancy migration, enabling stable configurations that enhance polarization stability and optimize interface conditions, ultimately contributing to higher conductance.

Our investigations reveal that repeated training pulses significantly enhance the durability of long-term plasticity in our device, effectively emulating biological synaptic learning and memory processes. This observed synaptic behavior is intrinsically linked to the heterostructure's multiferroic nature, where the coexistence of multiple ferroic orders introduces unique degrees of freedom and coupling mechanisms. This inherent multiferroicity contributes to the tunability and stability of synaptic responses, enabling the device to mimic complex biological learning and memory functions and precisely control the postsynaptic current response. The choice of the Cr-doped $\text{SnO}_2/\text{Ti}_{0.6}\text{Sn}_{0.4}\text{O}_2/\text{TiO}_2$ heterostructure was pivotal for these capabilities. This design combines the ferromagnetic property of ultra-thin Cr-doped SnO_2 with the ferroelectric nature of $\text{Ti}_{0.6}\text{Sn}_{0.4}\text{O}_2$, forming a robust multiferroic foundation. Their structural similarity fosters a uniform interface, crucial for facilitating formation of 2DEG. Furthermore, ALD allowed precise control over layer thicknesses, confirming that the magnetoresistance is primarily interface-driven, peaking at just 10 nm for Cr-doped SnO_2 and 5–6 nm for $\text{Ti}_{0.6}\text{Sn}_{0.4}\text{O}_2$. This precision ensures robust magnetoelectric coupling at the interface, distinct from bulk properties, which underpins the tunable synaptic response. Critically, these oxide electronics are inherently CMOS-compatible, offering substantial advantages over other 2D materials for practical integration into scalable and efficient computing architectures. Ultimately, the demonstrated ability to

precisely control synaptic plasticity within this meticulously designed multiferroic heterostructure underscores its significant potential for developing sophisticated neuromorphic devices.

Experimental

Heterostructured semiconductor films were prepared on thermally oxidized silicon wafers ($\text{Si}/150\text{ nm SiO}_2$). The patterned Au/Cr substrates were deposited sequentially by electron-beam evaporation.⁸³ The first functional layer—approximately 9.0 nm of SnO_2 —was grown by plasma-enhanced atomic-layer deposition (PE-ALD) at 150 °C in flowing N_2 . Tetrakis (dimethylamino)tin(IV) ($\text{Sn} [(\text{CH}_3)_2\text{N}]_4$, TDMASn) (Sigma-Aldrich, 99.9%) served as the metal precursor, whereas O_2 plasma supplied the oxidant. Each ALD cycle (20 s) comprised a 5 s precursor pulse, the 5 s N_2 purge, 5 s O_2 -plasma exposure, and a final 5 s purge. Film thickness was tracked *in situ* by spectroscopic ellipsometry (J. A. Woollam M-2000), revealing excellent uniformity across 5-inch wafers. Selected SnO_2 coatings were then annealed at 400 °C for 10 min in nitrogen (heating rate 60 °C min^{-1}) to tailor their defect chemistry. Chromium incorporation was achieved *via* a supercycle approach, where each supercycle consisted of 5 cycles of SnO_2 deposition followed by 1 cycle(s) of chromium deposition. The chromium ALD cycle utilized chromium hexacarbonyl ($\text{Cr}(\text{CO})_6$), tris(2,4-pentanedionato)chromium(III) ($\text{Cr}(\text{thd})_3$), and tris(diethylamino)chromium(III) (TDEACr)] as the metal precursor and O_2 plasma as the coreactant. Then, the surface of the films was exposed to the titanium precursors. Subsequent deposition of the ultra-thin $\text{Ti}_x\text{Sn}_{1-x}\text{O}_2$ was also performed using a supercycle approach. Subsequently, a titanium dioxide (TiO_2) overlayer with a thickness of approximately 10 nm was deposited *via* PE-ALD using tetrakis(dimethylamido) titanium and O_2 plasma, with pulse durations of 0.1 s and 0.6 s, respectively. The fabricated films then underwent a thermal annealing treatment, after which the wafers were diced into $1 \times 1\text{ cm}^2$ chips for analysis.

Compositional and structural characterization employed X-ray photoelectron spectroscopy (Thermo Scientific Theta Probe) to determine chemical states and valence-band maxima, high-resolution X-ray diffraction (HRXRD, Rigaku SmartLab) to verify crystallinity before and after annealing, and aberration-corrected transmission electron microscopy (JEOL JEM-ARM 200F) and its EDS analyzer, SAED, EELS, and HAADF equipment (STEM JEM-ARM200F) energy-dispersive X-ray spectroscopy for atom-scale inspection of the interfaces. Cross-sectional lamellae were prepared by focused-ion-beam milling (Zeiss Crossbeam 540). Raman spectroscopy (HORIBA, LabRAM ARAMIS) was conducted using 532 nm lasers. Crystallinity was assessed *via* high-resolution X-ray diffraction (HRXRD, Rigaku SmartLab). Surface composition was analyzed by X-ray photoelectron spectroscopy (XPS, Thermo Scientific Theta Probe). Surface topography and nanopore morphology were characterized using atomic force microscopy (AFM, Park Systems NX10) with a Cr–Pt–Ir coated tip (radius of curvature $\approx 15.0\text{ nm}$, stiffness = 0.20 N m^{-1}). Conductive-AFM measurements were performed with a Cr/Pt/Ir-coated



probe (tip radius ≈ 15 nm, spring constant 0.20 N m $^{-1}$, resonance frequency 25 kHz); local I - V sweeps and current maps captured spatial variations in charge transport for the study of capacitive and memristive behavior of devices. The PFM (Park NX10) with a piezoelectric probe was used to characterize the piezoresponse of the heterostructured film. The KPFM setup was also employed for realizing the surface morphological characteristics and the measurements of the Fermi level energy of the samples.

Electrical transport and switching characterization. Electrical transport measurements were performed on Hall bar devices using a four-probe configuration. For electrical switching measurements, current pulses were applied to induce the switching process. Each pulse had a duration of 100 ms. Following the application of the pulse, a read current of 0.5 mA was applied, and the Hall voltage was measured to assess the device state. Standard Hall effect measurements were conducted using an Ecopia HMS-53000 system. Temperature- and field-dependent Hall effect measurements were performed using a quantum design physical property measurement system (PPMS) equipped with a ± 16 T superconducting magnet. Samples were mounted on a standard sample puck and cooled using the integrated closed-cycle helium cryostat, allowing measurements across a temperature range from 7.0 K to 300 K. For measurements of memristive and artificial synaptic characteristics, devices were fabricated on Au substrates. The device geometry consisted of depositing on the Au bottom electrode with Pt top electrodes deposited by a plasma sputtering technique. Memristive and artificial synaptic behavior was measured using a PGSTAT204 (Autolab Metrohm).

Conclusions

We report a multifunctional Cr-doped $\text{SnO}_2/\text{Ti}_{0.6}\text{Sn}_{0.4}\text{O}_2/\text{TiO}_2$ 2D heterostructure with unique coexistence of ferroelectric, ferromagnetic and gate-tunable 2DEG capabilities at the oxide interfaces. Detailed structural and spectroscopic analyses have confirmed the interfacial elemental diffusion, oxygen vacancy formation and mixed-valence Ti^{3+} states, which in turn collectively drive the electronic reconstruction and 2DEG formation. The Hall effect measurements confirmed the n-type carriers with high mobility ($\sim 1.7 \times 10^3$ cm 2 V $^{-1}$ s $^{-1}$ at 7.0 K), accompanied by the temperature-dependent metal-insulator transitions and clear Shubnikov-de Haas oscillations, confirming the quantum transport behavior. Moreover, the fabricated 2D heterostructures have shown AHE and negative magnetoresistance indicating the robust spin-polarized transport and magnetic ordering persisting up to room temperature. Crucially, a capacitive-to-inductive transition in the memristive I - V behavior has been observed suggesting the dynamic ionic and magnetic interactions. The device based on fabricated 2D heterostructures exhibited analogue, multi-level resistive switching, low threshold voltages and spike-rate-dependent plasticity, enabling the emulation of biological synaptic functions for neuromorphic computing. Thus, all these findings

established a scalable oxide-based nano-platform that combines the quantum transport, spin-orbit interactions and ferroelectric control, offering a promising route towards the field-free spintronic switching, chiral spin texture engineering and the next-generation neuromorphic nanoarchitectures.

Author contributions

M. K. Akbari conceived and designed the study, synthesized the heterostructures by ALD, carried out all structural and electrical characterizations, and evaluated device performance. The fabrication and subsequent materials characterization were conducted through a collaborative effort between the Melbourne Centre for Nanofabrication and the CoCOON Core Facility at Ghent University, indicating that key stages of both the device fabrication and the comprehensive material analyses were performed utilizing the resources and expertise of both centers. All three-dimensional renderings were generated by M. K. Akbari. M. K. Akbari, C. Detavernier, Y. Cui, and S. Zhuiykov jointly interpreted the data and contributed to manuscript preparation. S. Zhuiykov provided overall project supervision. All authors reviewed and approved the final manuscript.

Conflicts of interest

There are no conflicts to declare.

Data availability

The data supporting this article have been included as part of the ESI.†

Acknowledgements

The work was supported by the Research & Development Program of the Ghent University Global Campus, South Korea. During the preparation of this work the authors used “gemini-1.5-pro” to check the grammar and spelling. After using this tool, the authors reviewed and edited the content as needed and take full responsibility for the content of the publication. For data analysis, authors used Python. The 3D graphical schemes were specifically designed by “Blender” software.

References

- 1 S. Stemmer and S. J. Allen, *Annu. Rev. Mater. Res.*, 2014, **44**, 151–171.
- 2 R. Yang, H. Yin, M. Li, S. Wang and K. Jin, *ACS Appl. Electron. Mater.*, 2022, **4**, 1117–1123.
- 3 X. Guo, L. Zhou, B. Roul, Y. Wu, Y. Huang, S. Das and Z. Hong, *Small*, 2022, **18**, 2200486.
- 4 Y.-T. Shao, S. Das, Z. Hong, R. Xu, S. Chandrika, F. Gómez-Ortiz, P. García-Fernández, L.-Q. Chen, H. Y. Hwang, J. Junquera, L. W. Martin, R. Ramesh and D. A. Muller, *Nat. Commun.*, 2023, **14**, 1355.



- 5 L. Hu, Y. Wu, Y. Huang, H. Tian and Z. Hong, *Nano Lett.*, 2023, **23**, 11353–11359.
- 6 S. Chen, S. Yuan, Z. Hou, Y. Tang, J. Zhang, T. Wang, K. Li, W. Zhao, X. Liu, L. Chen, L. W. Martin and Z. Che, *Adv. Mater.*, 2021, **33**, 2000857.
- 7 P. Gao, J. Britson, J. R. Jokisaari, C. T. Nelson, S.-H. Baek, Y. Wang, C.-B. Eom, L.-Q. Chen and X. Pan, *Nat. Commun.*, 2013, **4**, 2791.
- 8 J. Seidel, *Nat. Mater.*, 2019, **18**, 188–190.
- 9 D. Wang, S. Hao, B. Dkhil, B. Tian and C. Duan, *Fundam. Res.*, 2024, **4**, 1272–1291.
- 10 P. Behera, M. A. May, F. Gómez-Ortiz, S. Susarla, S. Das, C. T. Nelson, L. Caretta, S.-L. Hsu, M. R. McCarter, B. H. Savitzky, E. S. Barnard, A. Raja, Z. Hong, P. García-Fernandez, S. W. Lovesey, G. van der Laan, P. Ercius, C. Ophus, L. W. Martin, J. Junquera, M. B. Raschke and R. Ramesh, *Sci. Adv.*, 2022, **8**, eabj8030.
- 11 J. P. Barnard, J. Shen, Y. Zhang, J. Lu, J. Song, A. Siddiqui, R. Sarma and H. Wang, *Nanoscale Adv.*, 2023, **5**, 5850–5858.
- 12 M. C. Sulzbach, H. Tan, S. Estandía, J. Gàzquez, F. Sánchez, I. Fina and J. Fontcuberta, *ACS Appl. Electron. Mater.*, 2021, **3**, 3657–3666.
- 13 I. Olaniyan, I. Tikhonov, V. V. Hevelke, S. Wiesner, L. Zhang, A. Razumnaya, N. Cherkashin, S. Schamm-Chardon, I. Lukyanchuk, D.-J. Kim and C. Dubourdieu, *Nat. Commun.*, 2024, **15**, 10047.
- 14 J. Fowlie, A. Karn and C. Cancellieri, *et al.*, *ACS Nano*, 2021, **15**, 14937–14948.
- 15 H. K. Chung, J. J. Pyeon, I.-H. Baek, G.-Y. Lee, H. Lee, S. O. Won, J. H. Han, T.-M. Chung, T. J. Park and S. K. Kim, *J. Vac. Sci. Technol., A*, 2020, **38**, 012404.
- 16 L. Rykkje, O. Nilsen and H. H. Sønsteby, *ACS Appl. Electron. Mater.*, 2025, **7**, 2466–2475.
- 17 P. Sangeetha, V. Sasirekha and V. Ramakrishnan, *J. Raman Spectrosc.*, 2011, **42**, 1634–1639.
- 18 J. Zhou, M. S. Zhang, J. M. Hong, Z. Yin and Z. Yin, *Solid State Commun.*, 2006, **138**, 242–246.
- 19 Z. Hai, M. Karbalaei Akbari, Z. Wei, C. Xue, H. Xu, J. Hu, L. Hyde and S. Zhuiykov, *Mater. Today Commun.*, 2017, **12**, 55–62.
- 20 J. C. R. Aquino, F. H. Aragón, J. A. Coaquira, X. Gratens, V. A. Chitta, I. Gonzales, W. A. A. Macedo and P. C. Morais, *J. Phys. Chem. C*, 2017, **121**, 21670–21677.
- 21 H.-X. Luan, C.-W. Zhang, F. Li, P. Li, M.-J. Ren, M. Yuan, W.-X. Ji and P.-J. Wang, *RSC Adv.*, 2014, **4**, 9602–9607.
- 22 L. Zhang, S. Ge, Y. Zuo, J. Wang and J. Qi, *Scr. Mater.*, 2010, **63**, 953–956.
- 23 L. Diehl, S. Bette, F. Pielnhöfer, S. Betzler, I. Moudrakovski, G. A. Ozin, R. Dinnebir and B. V. Lotsch, *Chem. Mater.*, 2018, **30**, 8932–8938.
- 24 J. Gardner, A. Thakre, A. Kumar and J. F. Scott, *Rep. Prog. Phys.*, 2019, **82**, 092501.
- 25 N. Kumada, Y. Yonesaki, T. Takei, N. Kinomura and S. Wada, *Mater. Res. Bull.*, 2009, **44**, 1298–1300.
- 26 R. Agarwal, Y. Sharma, S. Chang, K. C. Pitike, C. Sohn, S. M. Nakhmanson, C. G. Takoudis, H. N. Lee and R. Tonelli, *Phys. Rev. B*, 2018, **97**, 054109.
- 27 Y. Worku, D. R. Sahu and V. V. Srinivasu, *Magnetic Materials and Magnetic Levitation*, IntechOpen, 2021.
- 28 L. Xu, Z. Wu, Y. Han, M. Wang, J. Li, C. Chen, L. Wang, Y. Yuan, L. Shi, J. M. Redwing and X. Zhang, *Nano Lett.*, 2025, **25**, 8423–8430.
- 29 T. Hirata, *J. Am. Ceram. Soc.*, 2000, **83**, 3205–3207.
- 30 Y. Uratani, T. Shishidou and T. Oguchi, *Jpn. J. Appl. Phys.*, 2008, **47**, 7735–7739.
- 31 W. D. Parker, J. M. Rondinelli and S. M. Nakhmanson, *Phys. Rev. B: Condens. Matter Mater. Phys.*, 2011, **84**, 245126.
- 32 S. F. Matar, I. Baraille and M. A. Subramanian, *Chem. Phys.*, 2009, **355**, 43–48.
- 33 F. W. Dynys, M.-H. Berger and A. Sehirlioglu, *J. Am. Ceram. Soc.*, 2012, **95**, 619–626.
- 34 N. Siedl, S. O. Baumann, M. J. Elser and O. Diwald, *J. Phys. Chem. C*, 2012, **116**, 22967–22973.
- 35 A. F. Santander-Syro, C. Bareille, F. Fortuna, O. Copie, A. Taleb Ibrahim, P. Le Fèvre, F. Bertran, T. Merz, O. V. Yazyev, H. Y. Hwang and F. Baumberger, *Nat. Mater.*, 2014, **13**, 1085–1090.
- 36 P. Pascariu, C. Cojocar, M. Homocianu, P. Samoila, C. Romanitan and N. Djourellov, *Ceram. Int.*, 2023, **49**, 10384–10394.
- 37 Y. Cao, T. He, L. Zhao, E. Wang, W. Yang and Y. Cao, *J. Phys. Chem. C*, 2009, **113**, 18121–18124.
- 38 A. Walsh, D. J. Payne, R. G. Egdell and G. W. Watson, *Chem. Soc. Rev.*, 2011, **40**, 4455.
- 39 L. Diehl, D. H. Fabini, N. M. Vargas-Barbosa, A. Jiménez-Solano, T. Block, V. Duppel, I. Moudrakovski, K. Küster, R. Pöttgen and B. V. Lotsch, *Chem. Mater.*, 2021, **33**, 2824–2836.
- 40 M. Emam-Ismael, A. A. Gharieb, S. H. Moustafa, M. M. Mahasen, E. R. Shaaban and M. El-Hagary, *J. Phys. Chem. Solids*, 2021, **157**, 110195.
- 41 I. M. Costa, T. R. Cunha, L. Cichetto Jr., M. A. Zaghet and A. J. Chiquito, *Phys. E*, 2021, **134**, 114856.
- 42 M. B. Ghasemian, A. Zavabeti, F.-M. Allieux, P. Sharma, M. Mousavi, M. A. Rahim, R. K. Nekouei, J. Tang, A. J. Christofferson, N. Meftahi, S. Rafiezadeh, S. Cheong, P. Koshy, R. D. Tilley, C. F. McConville, S. P. Russo, C. Ton-That, J. Seidel and K. Kalantar-Zadeh, *Small*, 2024, **20**, 2309924.
- 43 D. Xiao, W. Zhu, Y. Ran, N. Nagaosa and S. Okamoto, *Nat. Commun.*, 2011, **2**, 596.
- 44 N. Kelaidis, A. Kordatos, S. R. Christopoulos and A. Chronos, *Sci. Rep.*, 2018, **8**, 12790.
- 45 S. F. Rus, T. Z. Ward and A. Herklotz, *Thin Solid Films*, 2016, **615**, 103–106.
- 46 D. G. Schlom, L.-Q. Chen, X. Pan, A. Schmehl and M. A. Zurbuchen, *J. Am. Ceram. Soc.*, 2008, **91**, 2429–2454.
- 47 Y. Wang, Q. He, W. Ming, M.-H. Du, N. Lu, C. Cafolla, J. Fujioka, Q. Zhang, D. Zhang, S. Shen, Y. Lyu, A. T. N'Diaye, E. Arenholz, L. Gu, C. Nan, Y. Tokura and S. Okamoto, *Phys. Rev. X*, 2020, **10**, 021030.
- 48 Z. He, Q. Yang, G. Xi, J. Tu, J. Tian and L. Zhang, *Appl. Surf. Sci.*, 2023, **625**, 157193.



- 49 J. Bréhin, F. Trier, L. M. Vicente-Arche, P. Hemme, P. Noël, M. Cosset-Chéneau, J.-P. Attané, L. Vila and A. Sander, *Phys. Rev. Mater.*, 2020, **4**, 041002.
- 50 Y. Chen, N. Pryds, J. E. Kleibeuker, G. Koster, J. Sun, E. Stamate, B. Shen, G. Rijnders and S. Linderoth, *Nano Lett.*, 2011, **11**, 3774–3778.
- 51 T. J. Seok, Y. Liu, J. H. Choi, H. J. Kim, D. H. Kim, S. M. Kim, J. H. Jang, D.-Y. Cho, S. W. Lee and T. J. Park, *Chem. Mater.*, 2020, **32**, 7662–7669.
- 52 P. Sharma, S. Ryu, J. D. Burton, T. R. Paudel, C. W. Bark, Z. Huang, E. Y. Tsymbal, G. Catalan, C. B. Eom and A. Gruverman, *Nano Lett.*, 2015, **15**, 3547–3551.
- 53 S. W. Lee, *J. Nanomater.*, 2016, 1671390.
- 54 S. Y. Lee, J. Kim, A. Park, J. Park and H. Seo, *ACS Appl. Electron. Mater.*, 2024, **6**, 3613–3620.
- 55 Y. Jang, D. Jung, P. R. Sultane and C. W. Bielawski, *Appl. Surf. Sci.*, 2022, **600**, 154103.
- 56 J. Bréhin, Y. Chen, M. D'Antuono, S. Varotto, D. Stornaiuolo, C. Piamonteze, J. Varignon, M. Salluzzo and M. Bibes, *Nat. Phys.*, 2023, **19**, 823–829.
- 57 M. G. Kang, S. Lee and B. G. Park, *npj Spintronics*, 2025, **3**, 8.
- 58 F. Y. Bruno, M. N. Grisolia, C. Visani, S. Valencia, M. Varela, R. Abrudan, J. Tornos, A. Rivera-Calzada, A. A. Ünal, S. J. Pennycook, Z. Sefrioui, C. Leon, J. E. Villegas, J. Santamaria, A. Barthélémy and M. Bibes, *Nat. Commun.*, 2015, **6**, 6306.
- 59 J.-Y. Yoon, Y. Takeuchi, R. Takechi, J. Han, T. Uchimura, Y. Yamane, S. Kanai, J. Ieda, H. Ohno and S. Fukami, *Nat. Commun.*, 2025, **16**, 1171.
- 60 S. Bansal, S. C. Kashyap and D. K. Pandya, *J. Alloys Compd.*, 2015, **646**, 483–489.
- 61 K. Takahashi, C. R. W. Steward, M. Ogata, R. M. Fernandes and J. Schmalian, *arXiv*, 2025, preprint, arXiv:2502.03517, DOI: [10.48550/arXiv.2502.03517](https://doi.org/10.48550/arXiv.2502.03517).
- 62 A. Tao, Y. Jiang, S. Chen, Y. Zhang, Y. Cao, T. Yao, C. Chen, H. Ye and X.-L. Ma, *Nat. Commun.*, 2024, **15**, 6099.
- 63 M. L. Savchenko, J. Gospodaric, A. Shuvaev, I. A. Dmitriev, V. Dziom, A. A. Dobretsova, N. N. Mikhailov, Z. D. Kvon and A. Pimenov, *Phys. Rev. Res.*, 2024, **6**, L022027.
- 64 T. Miyasato, N. Abe, T. Fujii, A. Asamitsu, S. Onoda, N. Nagaosa and Y. Tokura, *Phys. Rev. Lett.*, 2007, **99**, 086602.
- 65 F. Risch, P. Koutsogiannis, Y. Tikhonov, A. G. Razumnaya, C. Magén, J. A. Pardo, I. Lukyanchuk and I. Stolichnov, *ACS Nano*, 2025, **19**, 6993–7004.
- 66 Q. Liu, S. Cui, R. Bian, E. Pan, G. Cao, W. Li and F. Liu, *ACS Nano*, 2024, **18**, 1778–1819.
- 67 J. Du, B. Sun, C. Yang, Z. Cao, G. Zhou, H. Wang and Y. Chen, *Mater. Today Phys.*, 2025, **50**, 101607.
- 68 C. Gonzales, A. Guerrero and J. Bisquert, *J. Phys. Chem. C*, 2022, **126**, 13560–13578.
- 69 A. Bou, C. Gonzales, P. P. Boix, Y. Vaynzof, A. Guerrero and J. Bisquert, *J. Phys. Chem. Lett.*, 2025, **16**, 69–76.
- 70 M. Berruet, J. C. Pérez-Martínez, B. Romero, C. Gonzales, A. M. Al-Mayouf, A. Guerrero and J. Bisquert, *ACS Energy Lett.*, 2022, **7**, 1214–1222.
- 71 H. S. Dehsari, M. H. Amiri and K. Asadi, *ACS Nano*, 2023, **17**, 8064–8073.
- 72 J. F. Scott, *Ferroelectric Memories*, Springer, 2000.
- 73 A. K. Tagantsev, L. E. Cross and J. Fousek, *Domains in Ferroic Crystals and Thin Films*, Springer, 2002.
- 74 S. Ducharme, A. V. Bune, L. D. Poulsen, V. M. Gong and V. M. Fridkin, *Phys. Rev. B:Condens. Matter Mater. Phys.*, 2000, **62**, 12024.
- 75 X. Lou, *J. Appl. Phys.*, 2014, **116**, 044101.
- 76 R. Waser and M. Aono, *Nat. Mater.*, 2007, **6**, 833–840.
- 77 M. H. Lee, C. H. Lee, K. B. Kim, J. H. Kim and Y. S. Kim, *J. Appl. Phys.*, 2008, **103**, 014101.
- 78 K. Beom, Z. Fan, D. Li and N. Newman, *Mater. Today Phys.*, 2022, **24**, 100724.
- 79 G. Vats, J. Peräntie, J. Palosaari, J. Juuti, J. Seidel and Y. Bai, *ACS Appl. Electron. Mater.*, 2020, **2**(9), 2829–2836.
- 80 V. Boddu, F. Endres and P. Steinmann, *Sci. Rep.*, 2017, **7**, 806.
- 81 M. Yuan, *Phys. Chem. Chem. Phys.*, 2025, **27**, 7502–7518.
- 82 S. Dong, H. Liu, Y. Wang, J. Bian and J. Su, *ACS Appl. Mater. Interfaces*, 2024, **16**(15), 19235–19246.
- 83 H. Xu, M. Karbalaee Akbari, Z. Hai, Z. Wei, L. Hyde, F. Verpoort, C. Xue and S. Zhuiykov, *Mater. Des.*, 2018, **149**, 135–144.

